



OPEN

Correlation between structure, chromaticity, and dielectric properties of calcium copper pyrophosphates, $\text{Ca}_{2-x}\text{Cu}_x\text{P}_2\text{O}_7$

Rattana Baitahe^{1,2}, Chuchai Sronsri^{1,2}, Somphob Thompho^{3✉}, Kittichai Chaiseeda⁴, Nattaya Montri⁵ & Banjong Boonchom^{1,2✉}

The solid-state reaction was employed to synthesize $\text{Ca}_{2-x}\text{Cu}_x\text{P}_2\text{O}_7$ by varying the mole ratio between Ca and Cu. The structure and crystallography of the pyrophosphate compounds were identified and confirmed by using X-ray diffraction (XRD). The Rietveld refinement method and the extended X-ray absorption fine structure (EXAFS) least-squares fitting technique were also applied to refine the sample crystal structure. The single phases of the obtained $\text{Ca}_2\text{P}_2\text{O}_7$, CaCuP_2O_7 , and $\text{Cu}_2\text{P}_2\text{O}_7$ samples and the mixing phases of the obtained $\text{Ca}_{1.5}\text{Cu}_{0.5}\text{P}_2\text{O}_7$ and $\text{Ca}_{0.5}\text{Cu}_{1.5}\text{P}_2\text{O}_7$ samples were identified, and then only a single phase of the samples was subjected to structural and dielectrical analyses. The structural results exhibit the tetragonal crystal system with the $P4_1$ space group for $\beta\text{-Ca}_2\text{P}_2\text{O}_7$, the monoclinic crystal system with the $P2_1/c$ space group for CaCuP_2O_7 , and the $C2/c$ space group for $\alpha\text{-Cu}_2\text{P}_2\text{O}_7$. The dielectric constant (ϵ_r) of the single metal pyrophosphates ($\text{Ca}_2\text{P}_2\text{O}_7$ and $\text{Cu}_2\text{P}_2\text{O}_7$) was higher than that of binary metal pyrophosphates (CaCuP_2O_7). The image sensor result of the $\text{Cu}_2\text{P}_2\text{O}_7$ sample ($x = 2.00$) illustrated a yellowish-green color, while other compounds ($x = 0.50\text{--}1.50$) presented color tones that changed from blue-green to bluish-green. Raman and Fourier transform infrared (FTIR) spectrophotometers were employed to characterize and confirm the vibrational characteristics of the $\text{P}_2\text{O}_7^{4-}$ group, which contains the O–P–O radical ($[\text{PO}_2]^-$) and the P–O–P bridge ($[\text{OPO}]^-$) and approximate M–O stretching modes. Furthermore, this work reports for the first time that the change in the crystal structure of $\text{Ca}_{2-x}\text{Cu}_x\text{P}_2\text{O}_7$ (i.e., bond angle of P–O–P in $\text{P}_2\text{O}_7^{4-}$ and distortion phenomena in the M–O₆ octahedral site) are cause the correlation between the structure, chromaticity, and dielectric properties of calcium copper pyrophosphates, $\text{Ca}_{2-x}\text{Cu}_x\text{P}_2\text{O}_7$.

Currently, metal phosphate materials show interesting properties because they are used in many applications. For example, they have been applied as microwave dielectric materials, corrosion-resistant coatings, biomedical cements, chelating agents, glass ceramics, and high-quality fertilizers^{1–3}. Bian et al.² reported that metal pyrophosphates ($M_2\text{P}_2\text{O}_7$, $M = \text{divalent cations}$) show low-loss dielectric properties as well as a relatively low sintering temperature. When the ionic radius of M in the $M_2\text{P}_2\text{O}_7$ structure is higher than 0.97 Å ($M = \text{Ca}^{2+}, \text{Sr}^{2+}, \text{Ba}^{2+}, \text{Pb}^{2+}, \text{Cd}^{2+}$)⁴, $M_2\text{P}_2\text{O}_7$ compounds crystallize in the dichromate ($\text{Cr}_2\text{O}_7^{2-}$) form, in which a pair of $\text{P}_2\text{O}_7^{4-}$ groups in eclipsed are the center of symmetry and bridging oxygen (O) atoms spread to each other. However, when the ionic radius of M is lower than 0.97 Å ($M = \text{Ni}^{2+}, \text{Mg}^{2+}, \text{Zn}^{2+}, \text{Co}^{2+}, \text{Cu}^{2+}, \text{Mn}^{2+}$), the $M_2\text{P}_2\text{O}_7$ structure is a thortveitite type⁵ (scandium yttrium silicate ($\text{Sc,Y})_2\text{Si}_2\text{O}_7$ with the monoclinic crystal system, prismatic crystal class ($2/m$), and $C2/m$ space group⁶). Based on this thortveitite structure, $\text{P}_2\text{O}_7^{4-}$ groups occur in a staggered conformation. Moreover, compared to metal oxides (i.e., MO , $M = \text{divalent metals}$), thortveitite-type pyrophosphates, such as

¹Material Science for Environmental Sustainability Research Unit, School of Science, King Mongkut's Institute of Technology Ladkrabang, Bangkok 10520, Thailand. ²Municipal Waste and Wastewater Management Learning Center, School of Science, King Mongkut's Institute of Technology Ladkrabang, Bangkok 10520, Thailand. ³Pharmaceutical Research Instrument Center, Faculty of Pharmaceutical Sciences, Chulalongkorn University, Pathumwan, Bangkok 10330, Thailand. ⁴Organic Synthesis, Electrochemistry and Natural Product Research Unit (OSEN), Department of Chemistry, Faculty of Science, King Mongkut's University of Technology Thonburi, Bangkok 10140, Thailand. ⁵Department of Plant Production Technology, School of Agricultural Technology, King Mongkut's Institute of Technology Ladkrabang, Bangkok 10520, Thailand. ✉email: somphob@hotmail.com; banjong.bo@kmitl.ac.th

α - $\text{Cu}_2\text{P}_2\text{O}_7$ and α - $\text{Mg}_2\text{P}_2\text{O}_7$, exhibit a rather low sintering temperature. However, the single metal pyrophosphate groups, such as $\text{Cu}_2\text{P}_2\text{O}_7$, $\text{Mg}_2\text{P}_2\text{O}_7$, $\text{Zn}_2\text{P}_2\text{O}_7$, and $\text{Co}_2\text{P}_2\text{O}_7$, still show a phase transition with changing sintering temperature. Therefore, the first aim of this research is to modify the crystal structures of some metal pyrophosphate compounds to decrease the loss of the dielectric value, manipulate the relative permittivity with various temperatures, and improve the stability of the crystal structure in the high-temperature range.

The crystal structures of $M_2\text{P}_2\text{O}_7$ compounds have been extensively investigated, and some metal pyrophosphates exhibit the allotropic property (a property of some compounds to exist in two or more crystal forms). For example, β - $\text{Ca}_2\text{P}_2\text{O}_7$ is tetragonal, whereas α - $\text{Ca}_2\text{P}_2\text{O}_7$ is monoclinic⁷. $\text{Ca}_2\text{P}_2\text{O}_7$ is also an important material in the luminescence⁸ and biomaterial⁹ fields. The thortveitite form undergoes a reversible phase transformation below 600 °C from the α -form (occurring at low temperature) to the β -form (occurring at high temperature). However, the dichromate form undergoes irreversible transformation at temperatures above 700 °C. The thortveitite-form $M_2\text{P}_2\text{O}_7$ ($M = \text{Mg}^{2+}$, Mn^{2+} , and Zn^{2+}) compounds are difficult to sinter into dense ceramics⁵. SrZnP_2O_7 , CaZnP_2O_7 , α - $\text{Zn}_2\text{P}_2\text{O}_7$, SrCuP_2O_7 , $\text{Mn}_2\text{P}_2\text{O}_7$, and CaCuP_2O_7 are effective glass-free low-temperature co-fired ceramic (LTCC) materials^{2,10,11}. All these metal pyrophosphates react with silver (Ag), but CaZnP_2O_7 and SrZnP_2O_7 do not react with copper (Cu)⁵.

Unary metal pyrophosphate, such as $\text{Mg}_2\text{P}_2\text{O}_7$, was thermally synthesized by using minerals such as dittmarite ($\text{NH}_4\text{MgPO}_4 \cdot \text{H}_2\text{O}$), struvite ($\text{NH}_4\text{MgPO}_4 \cdot 6\text{H}_2\text{O}$), and newberyite ($\text{MgHPO}_4 \cdot 3\text{H}_2\text{O}$) as precursors¹². Binary metal pyrophosphates, such as $\text{Mn}_{1.8}\text{Co}_{0.2}\text{P}_2\text{O}_7$, were synthesized from the thermal decomposition of manganese cobalt hydrogen phosphate trihydrate ($\text{Mn}_{0.9}\text{Co}_{0.1}\text{HPO}_4 \cdot 3\text{H}_2\text{O}$)¹³. Another binary metal compound, CaCuP_2O_7 , was synthesized by using a mixture of diammonium hydrogen phosphate ($(\text{NH}_4)_2\text{HPO}_4$), calcium carbonate (CaCO_3), and copper oxide (CuO) with the losses of carbon dioxide (CO_2) and ammonia (NH_3) gases based on the following equation (Eq. (1))¹⁴:



To decompose the carbonate (CO_3^{2-}) and condense the phosphate (PO_4^{3-}), resulting in the formation of pyrophosphate ($\text{P}_2\text{O}_7^{4-}$), the solid-state starting materials ($(\text{NH}_4)_2\text{HPO}_4 + \text{CaCO}_3 + \text{CuO}$) were homogeneously mixed first and kept at 700 °C. The obtained mixture was ground and then kept at 1060 °C for nine days. Using this thermal decomposition reaction, CaCuP_2O_7 was successfully synthesized. In addition, manganese cobalt magnesium hydrogen phosphate trihydrate ($\text{Mn}_{0.90}\text{Co}_{0.05}\text{Mg}_{0.05}\text{HPO}_4 \cdot 3\text{H}_2\text{O}$)¹⁵, manganese cobalt magnesium pyrophosphate dihydrate ($\text{Mn}_{1.8}\text{Co}_{0.1}\text{Mg}_{0.1}\text{P}_2\text{O}_7 \cdot 2\text{H}_2\text{O}$)¹⁶, and ammonium cobalt zinc manganese monohydrate ($\text{NH}_4\text{Co}_{0.8}\text{Zn}_{0.1}\text{Mn}_{0.1}\text{PO}_4 \cdot \text{H}_2\text{O}$)¹⁷ were employed as precursors to synthesize ternary metal pyrophosphates, namely, $\text{Mn}_{1.8}\text{Co}_{0.1}\text{Mg}_{0.1}\text{P}_2\text{O}_7$, $\text{Mn}_{1.8}\text{Co}_{0.1}\text{Mg}_{0.1}\text{P}_2\text{O}_7$, and $\text{Co}_{1.6}\text{Zn}_{0.2}\text{Mn}_{0.2}\text{P}_2\text{O}_7$, respectively.

Most studies of different metal phosphate and metal pyrophosphate compounds have focused on both the syntheses and the characterizations of bulk^{18,19} and nano particles^{20,21}, the kinetics and thermodynamics of the reaction^{22,23}, and their properties^{24,25}. For example, the photoluminescence of the $\text{LiMg}_{0.74}\text{Mn}_{0.26}\text{PO}_4$ phosphor was investigated, and the results revealed that the luminescent property of this phosphor depended on its surface area²⁶. Nevertheless, the relationship between crystal structures and dielectric properties is not widely understood. Therefore, the second aim of this work is to investigate the influence of the crystal structure on the dielectric phenomena of binary metal pyrophosphate compounds. Furthermore, substitutional solid solutions (binary metal compounds) based on the Hume-Rothery rules can be formed if the solute (Ca^{2+}) and solvent (Cu^{2+} of $\text{Cu}_2\text{P}_2\text{O}_7$) have similar valency ($\text{Cu} = \text{Ca} = 2+$) and the same crystal structure (β - $\text{Cu}_2\text{P}_2\text{O}_7 = \alpha$ - $\text{Ca}_2\text{P}_2\text{O}_7 = \text{monoclinic}$). This information shows a high possibility of substitutional metals between Cu and Ca ions forming a binary metal solid solution in pyrophosphate compounds, i.e., $\text{Ca}_{2-x}\text{Cu}_x\text{P}_2\text{O}_7$.

The dielectric properties of metal pyrophosphates occur due to two effects. They comprise the movement of M^{2+} ions in the MO_6 octahedral and the shifting of O atoms in the collinear P–O–P bridge of the $\text{O}_3\text{P–O–PO}_3$ or $\text{P}_2\text{O}_7^{4-}$ anion. If the collinear P–O–P bond of $\text{P}_2\text{O}_7^{4-}$ is destroyed, some distortions will also occur in the MO_6 octahedra. This phenomenon will improve the dielectric properties of materials by polarization production²⁷. It is well known that the highly relative permittivity of BaTiO_3 tetragonal perovskite occurs from the Ti^{4+} ion off-centered in the TiO_6 octahedral.

The atomic radii of Cu^{2+} and Ca^{2+} are 0.73 and 1.00 Å, respectively, whereas their electronegativities are 1.90 and 1.00, respectively²⁸. Doping the large cationic species, i.e., Ca^{2+} , into the crystal structure of the $\text{Cu}_2\text{P}_2\text{O}_7$ host resulted in the formation of $\text{Ca}_{2-x}\text{Cu}_x\text{P}_2\text{O}_7$ solid solutions. Both distortion of the MO_6 octahedral and O shifting in the collinear P–O–P bond phenomena may occur. These phenomena may then improve the dielectric properties of Ca^{2+} -doped $\text{Cu}_2\text{P}_2\text{O}_7$ compounds at low sintering temperatures. Consequently, to investigate this doubt, this research synthesized $\text{Ca}_{2-x}\text{Cu}_x\text{P}_2\text{O}_7$ ($x = 0.00$ – 2.00) by using conventional and uncomplicated methods. Then, various scientific methods were used to characterize and confirm the synthesized $\text{Ca}_{2-x}\text{Cu}_x\text{P}_2\text{O}_7$ samples. Raman and Fourier transform infrared (FTIR) spectrophotometers were employed to characterize the vibrational spectra of the synthesized samples. X-ray diffraction (XRD) was used to investigate the crystal structure of the samples. The dielectric properties of the samples were also investigated by using an LCR meter, an effective technique for material measurement. The polarization phenomena in the crystal structure of the samples were studied to characterize the bond length and bond angle of $\text{Ca}_{2-x}\text{Cu}_x\text{P}_2\text{O}_7$. The chromaticity property was studied by applying the image sensor with a spatially multiplexed exposure-high dynamic range (SME-HDR) imaging function. The results were then compared to the CIE (International Commission on Illumination) chromaticity diagram (standard database). Consequently, these synthesized $\text{Ca}_{2-x}\text{Cu}_x\text{P}_2\text{O}_7$ compounds can be applied as effective optical materials. In addition, synchrotron light technology was also employed to analyze the $\text{Ca}_{2-x}\text{Cu}_x\text{P}_2\text{O}_7$ samples by using X-ray absorption spectroscopy (XAS) mode at the Cu and Ca K edges.

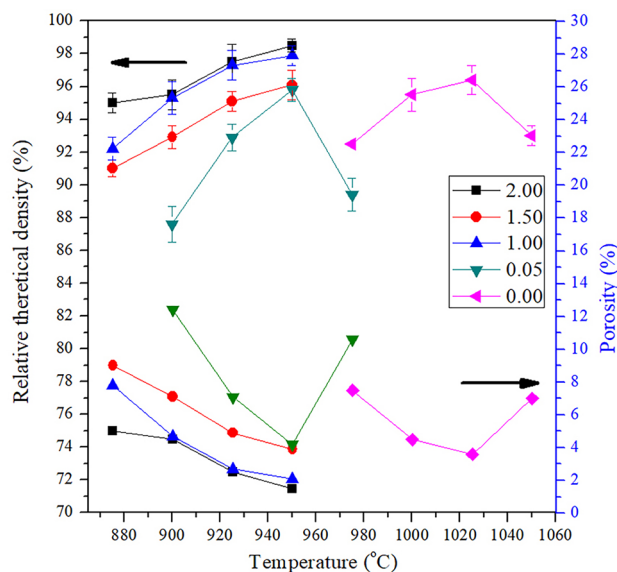
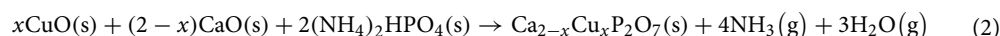


Figure 1. Relative theoretical densities (%) and porosities (%) of all prepared metal pyrophosphates ($\text{Ca}_{2-x}\text{Cu}_x\text{P}_2\text{O}_7$; $x=0.00\text{--}2.00$).

Materials and methods

Preparation. Binary metal pyrophosphate samples with various Ca/Cu ratios ($\text{Ca}_{2-x}\text{Cu}_x\text{P}_2\text{O}_7$, $x=0.00, 0.50, 1.00, 1.50$, and 2.00) were synthesized via the solid-state method. To avoid contamination, high-purity starting materials, namely, $(\text{NH}_4)_2\text{HPO}_4$ (99%), CuO (99.9%), and calcium oxide (CaO , 99.9%), were selected in this preparation process. All starting materials were weighed according to the stoichiometric ingredients and then homogenized by vibratory milling with 10 mm spherical yttria (yttrium oxide, Y_2O_3)-stabilized zirconia (zirconium dioxide, ZrO_2) (YSZ) grinding beads in ethanol media for 4 h. The dried powders were transferred to crucibles and directly heated at $1000\text{ }^\circ\text{C}$ for 24 h for $\text{Ca}_{2-x}\text{Cu}_x\text{P}_2\text{O}_7$, when $x=0.00\text{--}1.50$, and $800\text{ }^\circ\text{C}$ for 24 h for $\text{Ca}_{2-x}\text{Cu}_x\text{P}_2\text{O}_7$, when $x=2.00$. After that, the calcined powders were ball-milled anew, pressed uniaxially into small pellets at a pressure of $1000\text{ kg}\cdot\text{cm}^{-2}$ and then sintered at $950\text{ }^\circ\text{C}$ for 24 h for $\text{Ca}_{2-x}\text{Cu}_x\text{P}_2\text{O}_7$, when $x=0.00\text{--}1.50$, and $1030\text{ }^\circ\text{C}$ for 24 h for $\text{Ca}_{2-x}\text{Cu}_x\text{P}_2\text{O}_7$, when $x=2.00$. The observed densities of all prepared metal pyrophosphates, in theory, were investigated by Archimedes' principle and found to be in the range of 95–98% (Fig. 1). The preparation of the target powder samples ($\text{Ca}_{2-x}\text{Cu}_x\text{P}_2\text{O}_7$) was carried out according to the following reaction (Eq. (2)),



where $x=0.00\text{--}2.00$.

Characterization. The room temperature FTIR spectra of the samples were recorded by using a Perkin Elmer Spectrum GX FTIR spectrometer. The measured wavenumber range was $4000\text{--}400\text{ cm}^{-1}$, whereas the selected scan number and resolution were 8 scans and 4 cm^{-1} , respectively. A Thermo Scientific DXR Raman microscope was used to record the Raman spectra in the Raman shift of $1300\text{--}100\text{ cm}^{-1}$ using a scan number of 8 scans. A Raman spectrum was observed by irradiating each synthesized sample with an intense beam of an argon ion (Ar^+) laser with a wavenumber of $20,492\text{ cm}^{-1}$ (wavelength of 488 nm). The power of the incident beam was 12.5 mW. The XRD patterns of all prepared samples were recorded by using a D8 Advance X-ray diffractometer (XRD, Bruker AXS, Karlsruhe, Germany) with $\text{Cu K}\alpha$ radiation ($\lambda=0.1546\text{ nm}$) to analyze and confirm the crystal structures of the samples. The dielectric properties were analyzed as a function of the frequency ($1\text{--}1000\text{ kHz}$) and temperature (room temperature to $150\text{ }^\circ\text{C}$) using an Agilent/HP 4284A precision LCR meter (an effective technique for the material measurement with a wide frequency range ($20\text{ Hz--}1\text{ MHz}$) and superior signal performance to test materials to the most commonly used test standards). The Sony IMX214 CMOS image sensor (CIS, 13 MP "stacked" CIS with a spatially multiplexed exposure-high dynamic range (SME-HDR) imaging function) was applied to focus the colors of the samples. The results were then compared to the CIE (International Commission on Illumination) chromaticity diagram (standard database) to estimate the trend of the absorption wavelength. X-ray absorption spectroscopy (XAS) was performed at the Beamline 8 (BL8) Station of the National Synchrotron Research Center (NSRC, Nakhon Ratchasima, Thailand). BL8 of the NSRC is routinely operated for the XAS in an intermediate photon energy range from 1.25 to 10 keV^{29} . The double crystal $\text{Ge}(220)$ was used for the extended X-ray absorption fine structure (EXAFS) monochromator. The XAS spectra were detected in transmission mode at the copper (Cu) and calcium (Ca) K -edge.

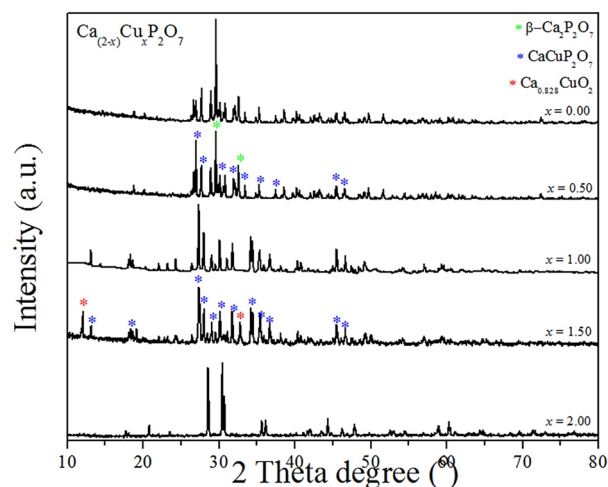


Figure 2. X-ray diffraction (XRD) patterns of the $\text{Ca}_{2-x}\text{Cu}_x\text{P}_2\text{O}_7$ powders ($x=0.00\text{--}2.00$) synthesized from the solid-state method of homogenized $(\text{NH}_4)_2\text{HPO}_4$, CuO , and CaO .

Ethics declarations.

- The datasets generated and/or analyzed during the current study are not available in the other repository.
- The datasets used and/or analyzed during the current study available from the corresponding author on reasonable request.
- All data generated or analyzed during this study are included in this published article.
- The datasets generated and/or analyzed during the current study are not publicly available due [REASON WHY DATA ARE NOT PUBLIC] but are available from the corresponding author on reasonable request.
- The data that support the findings of this study are available from the corresponding author but restrictions apply to the availability of these data, which were used under license for the current study, and so are not publicly available. Data are however available from the authors upon reasonable request and with permission of the corresponding author.

Results and discussion

Structural, optical, and dielectric analyses. After applying the D8 Advance X-ray diffractometer, the resulting XRD patterns of the synthesized $\text{Ca}_{2-x}\text{Cu}_x\text{P}_2\text{O}_7$ powders ($x=0.00\text{--}2.00$) are displayed in Fig. 2. The structures of $\text{Ca}_{2-x}\text{Cu}_x\text{P}_2\text{O}_7$ were analyzed through the Rietveld refinement analytic technique³⁰ using the Full-Prof package³¹. A pseudo-Voigt function (a linear combination between the Lorentzian and Gaussian functions) was adequate at all times for obtaining good fits of the experimental data. The initial model for the refinement of the single phase structure ($\text{Ca}_2\text{P}_2\text{O}_7$, CaCuP_2O_7 and $\text{Cu}_2\text{P}_2\text{O}_7$) was taken from parameters described well in the Calvo research³².

In addition, Fig. 3 shows the corresponding Rietveld refinement results of $\text{Ca}_{2-x}\text{Cu}_x\text{P}_2\text{O}_7$ when $x = 0.00, 1.00$, and 2.00 . Figure 3 shows the calculated (Y_{cal}) and observed (Y_{obs}) diffraction patterns as well as the different values between them ($Y_{\text{obs}} - Y_{\text{cal}}$) of the samples. The refinement plots gave the evolution of the XRD patterns in the various ratios between Ca and Cu ($\text{Ca}_{2-x}\text{Cu}_x\text{P}_2\text{O}_7$, $x = 0.00, 1.00$ and 2.00). The Rietveld refinement analysis and the XRD data of powders confirmed the formation of metal pyrophosphate compounds ($\text{Ca}_{2-x}\text{Cu}_x\text{P}_2\text{O}_7$).

The crystallographic information of the synthesized compounds is briefly described. When $x = 0.00$, the single metal pyrophosphate phase, $\beta\text{-Ca}_2\text{P}_2\text{O}_7$, was obtained with the tetragonal crystal system, space group of $P4_1$, space group number of 76, Schoenflies symbol of $C_4^{2,33}$, and number of formula units per unit cell or $Z = 8$. When $x = 1.00$, the binary metal pyrophosphate phase, CaCuP_2O_7 , was obtained with the monoclinic crystal system, space group of $P2_1/c$, space group number of 14, Schoenflies symbol of C_{2h}^5 , and $Z = 4$. Finally, when $x = 2.00$, another single metal pyrophosphate phase, $\alpha\text{-Cu}_2\text{P}_2\text{O}_7$, was obtained with the monoclinic crystal system, space group of $C2/c$, space group number of 15, Schoenflies symbol of C_{2h}^6 , and $Z = 4$. For other $\text{Ca}_{2-x}\text{Cu}_x\text{P}_2\text{O}_7$ samples, when $x = 0.50$, there were two phases between CaCuP_2O_7 and $\alpha\text{-Cu}_2\text{P}_2\text{O}_7$, whereas when $x = 1.50$, two phases between CaCuP_2O_7 and $\beta\text{-Ca}_2\text{P}_2\text{O}_7$ were then observed. The P–O–P bond angles (of the $\text{O}_3\text{P}-\text{O}-\text{PO}_3$ bridge of $\text{P}_2\text{O}_7^{4-}$) and $M-\text{O}_6$ bond lengths ($M = \text{Ca}$ or Cu) were determined by using refinement analysis, and the obtained values are summarized in Table 1.

X-ray absorption near-edge structure (XANES) is very sensitive to both the change in the local geometry (especially the ligand environment of the metal) and the oxidation state³⁴. Therefore, the spectra were collected at both the Ca and Cu K -edges. They could help to understand the Fourier transform evolutions³⁴. The X-ray absorption edge energies (E_0) of the synthesized $\text{Ca}_{2-x}\text{Cu}_x\text{P}_2\text{O}_7$ compounds at the Ca and Cu K -edges are listed in Table 2.

The E_0 values of the various Cu valences (Cu^0 , Cu^{1+} , and Cu^{2+}) obtained in this work are in line with the information reported by Yano and Yachandra³⁴. They reported that the E_0 values increase with increasing oxidation

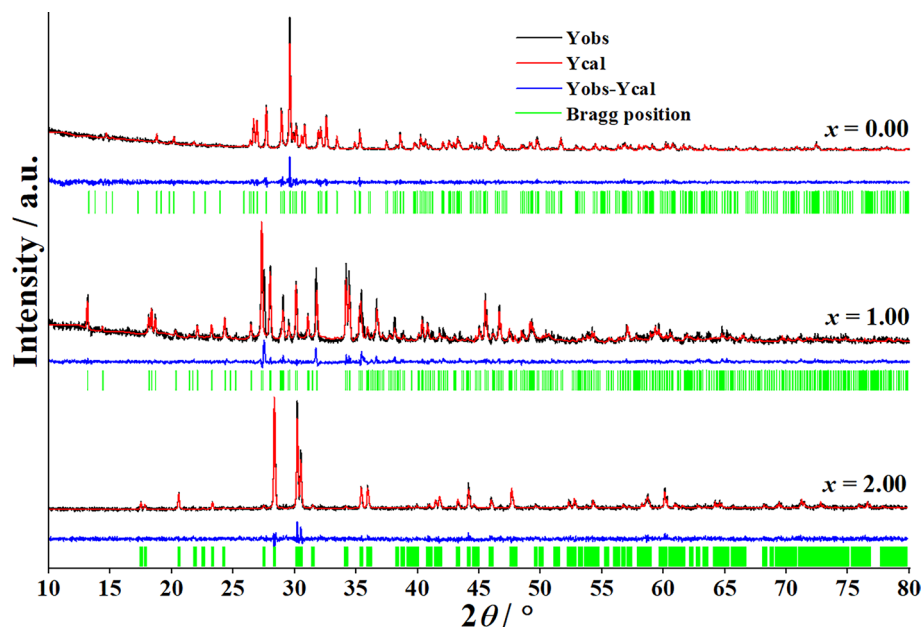


Figure 3. Rietveld refinement analytical results of the synthesized $\text{Ca}_{2-x}\text{Cu}_x\text{P}_2\text{O}_7$ samples when $x=0.00$, 1.00, and 2.00.

Samples	POP Angle (°)	M-O _x bond length (Å)				SG	Z	R _p	R _{wp}	R _{exp}	χ^2	
		Bonding	No. 1	No. 2	No. 3							No. 4
x = 2.00	154.60(10)	Cu-O _{eq}	1.886(5)	–	–	–	C2/c	4	0.093	0.117	0.107	1.2
		Cu-O _{eq}	1.942(6)	–	–	–						
		Cu-O _{eq}	1.980(5)	–	–	–						
		Cu-O _{eq}	1.995(5)	–	–	–						
		Cu-O _{ax}	2.354(9)	–	–	–						
		Cu-O _{ax}	2.920(9)	–	–	–						
x = 1.00	159.00(1)	Cu-O _{eq}	1.853(3)	–	–	–	P2 ₁ /n	4	0.094	0.130	0.077	2.86
		Cu-O _{eq}	2.004(2)	–	–	–						
		Cu-O _{eq}	2.106(1)	–	–	–						
		Cu-O _{eq}	2.129(5)	–	–	–						
		Cu-O _{ax}	2.245(3)	–	–	–						
		Cu-O _{ax}	2.811(1)	–	–	–						
x = 0.00	116.51(7) 140.96(1)	Ca-O1	2.53(5)	2.52(6)	2.55(4)	2.49(5)	P4 ₁	8	0.107	0.144	0.126	1.31
		Ca-O2	2.33(4)	2.60(5)	2.65(6)	2.19(4)						
		Ca-O3	2.50(5)	2.89(4)	2.61(5)	2.36(5)						
		Ca-O4	2.80(7)	2.16(6)	2.26(10)	2.56(7)						
		Ca-O5	2.36(4)	2.27(4)	2.26(4)	2.28(4)						
		Ca-O6	2.18(6)	2.30(4)	2.34(5)	2.53(5)						
		Ca-O7	2.91(4)	2.83(5)	2.50(4)	2.81(5)						

Table 1. Bond angles and bond lengths from the Rietveld refinement analytic technique for the synthesized $\text{Ca}_{2-x}\text{Cu}_x\text{P}_2\text{O}_7$ samples; $x=0.00$, 1.00, and 2.00. where eq and ax subscripts are the equatorial and axial (or apical) positions, respectively, and χ^2 is the goodness of fit. ND is not detected.

state. They also described that an electron in an atom experiences the full charge of the positive nucleus. In contrast, in the case of many electrons, the electrons in an outer layer are simultaneously repelled by the negatively charged electrons and attracted to the positive nucleus. The lower the oxidation state of metals is, the less positive the overall charge of the atom. Consequently, to excite an electron from an orbital, more energy is required. In summary, when the metal has a more positive charge, the E_0 values (XANES spectra) shift to a higher energy³⁴. According to Table 2, in the Cu K-edge, the E_0 values of the synthesized $\text{Ca}_{2-x}\text{Cu}_x\text{P}_2\text{O}_7$ samples ($x = 0.50$ – 2.00) were similar to the E_0 values of Cu^{2+}O , indicating that Cu^{2+} was monoclinic. In addition, the XANES spectra of

x values	Compounds	X-ray absorption edge energies (E_0) / electron Volt, eV	
		Ca K-edge	Cu K-edge
Cu ⁰	Cu ⁰	ND	8978.45
Cu ¹⁺	Cu ₂ O	ND	8979.52
Cu ²⁺	CuO	ND	8987.72
Ca ²⁺	CaO	4033.09	–
2.00	Cu ₂ P ₂ O ₇	ND	8987.88
1.50	Ca _{0.5} Cu _{1.5} P ₂ O ₇	4033.14	8987.08
1.00	CaCuP ₂ O ₇	4033.42	8987.09
0.50	Ca _{1.5} Cu _{0.5} P ₂ O ₇	4033.42	8987.13
0.00	Ca ₂ P ₂ O ₇	ND	ND

Table 2. X-ray absorption edge energies (E_0) of the synthesized Ca_{2-x}Cu_xP₂O₇ compounds when $x = 0.00$ – 2.00 . ND is not detected.

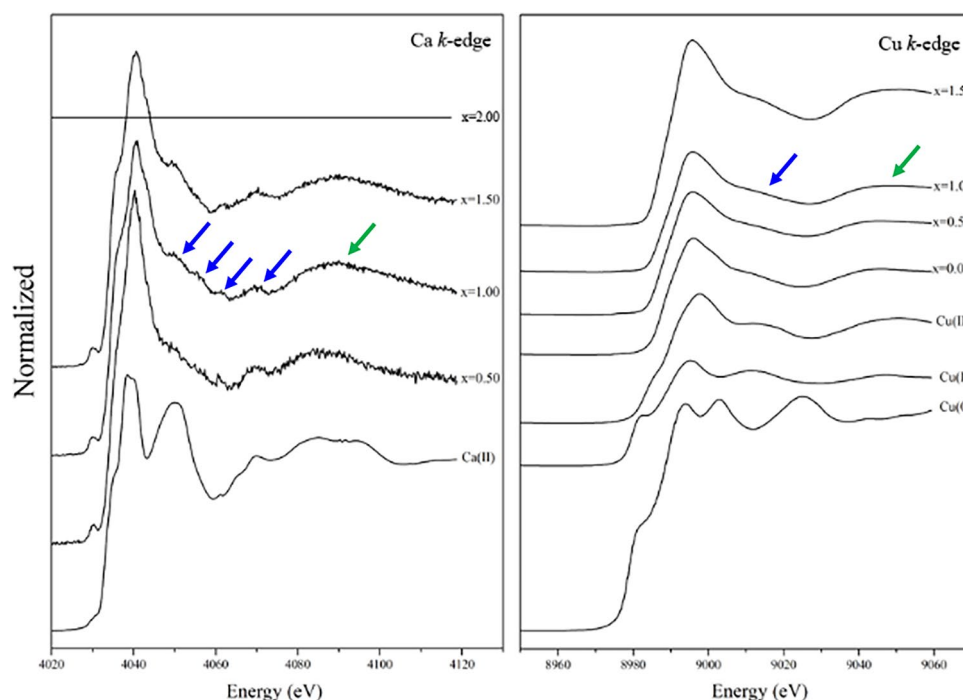


Figure 4. Local environment of Ca atoms when they entered the Cu₂P₂O₇ structure, resulting in the formation of Ca_{2-x}Cu_xP₂O₇.

samples in the Ca K-edge showed E_0 values similar to Ca²⁺O, indicating that there was Ca²⁺ in the crystal structure of the Cu₂P₂O₇ host, resulting in the formation of Ca_{2-x}Cu_xP₂O₇. Figure 4 presents the local environment of Ca atoms when they entered the Cu₂P₂O₇ structure. The spectra of Ca and Cu in the CaCuP₂O₇ compound were different. These results demonstrated that the coordinated environments of the divalent Ca in CaCuP₂O₇ are significantly different³⁵.

The coordinated complexes with different properties have different colors, such as blue for Cu(NH₃)₄H₂O)₂²⁺, red for Co(NH₃)₅H₂O)₃³⁺, and green for CoF₆³⁻. This different color phenomenon was well explained by the crystal field theory (CFT) described by El Jazouli et al. and Chen et al.^{36,37} The optical properties and the corresponding CIE chromatic coordinates^{36,38,39} of Ca_{2-x}Cu_xP₂O₇ samples ($x = 0.00$ – 2.00) are shown in Fig. 5. All Ca/Cu ratio compounds, except the composition with $x = 0.00$ (Ca₂P₂O₇), showed a greenish color, in which Ca₂P₂O₇ exhibited a colorless powder. The colors of the samples were dictated by the elongation or compression of the z ligand bonds of the Cu²⁺ ion. The result of the composition with $x = 2.00$ (Cu₂P₂O₇) illustrated a yellowish-green color, while the binary metal compounds ($x = 0.50$ – 1.50) presented color tones that changed from blue-green to bluish-green.

The mean static atomic dielectric constants (ϵ_r) of the synthesized Ca_{2-x}Cu_xP₂O₇ compounds were estimated using the well-known Clausius-Mossotti relation⁴⁰ as the following equation (Eq. (3)):

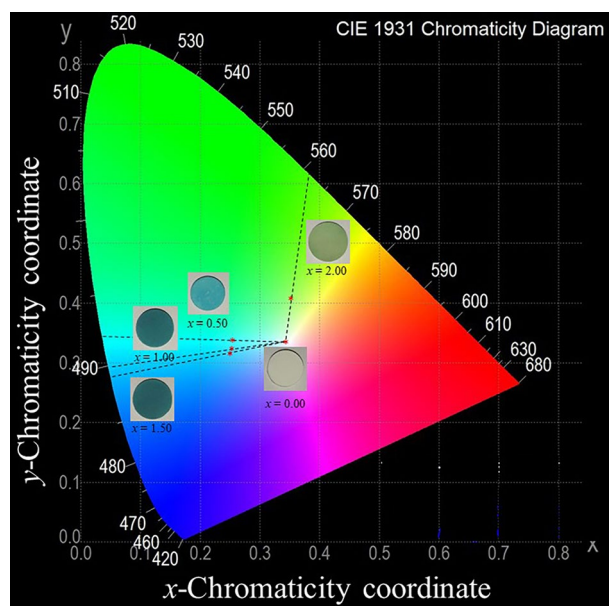


Figure 5. Optical properties and corresponding CIE (International Commission on Illumination) chromatic coordinates of $\text{Ca}_{2-x}\text{Cu}_x\text{P}_2\text{O}_7$; $x = 0.00\text{--}2.00$.

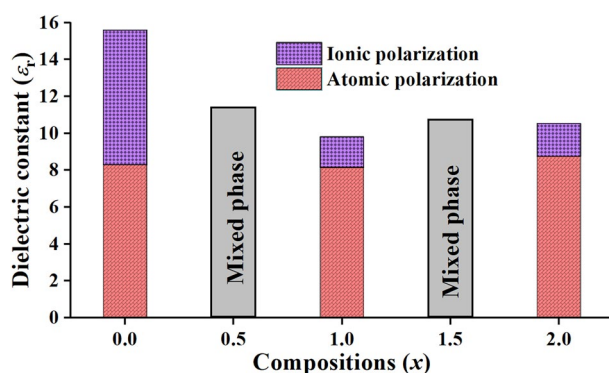


Figure 6. Dielectric constant as a function of the composition x of $\text{Ca}_{2-x}\text{Cu}_x\text{P}_2\text{O}_7$; $x = 0.00\text{--}2.00$.

$$\epsilon_r = \left(\frac{3V_m + 8\pi\alpha_D}{3V_m - 4\pi\alpha_D} \right) \quad (3)$$

where α_D is the sum of the dielectric polarizabilities of individual ions and V_m is the molar volume.

The effect of porosity on the permittivity was eliminated by applying Bosman and Havinga's correction⁴¹ as shown in Eq. (4), which can be used for some materials, i.e., dense ceramics, having porosities lower than 5%:

$$\epsilon_{r,\text{corrected}} = \epsilon_{r,\text{measured}}(1 + 1.5P) \quad (4)$$

where $\epsilon_{r,\text{measured}}$ and $\epsilon_{r,\text{corrected}}$ are the measured and corrected relative permittivity, respectively, and P is the fractional porosity.

After applying the Clausius-Mossotti relation (Eq. (3)), the dielectric constant (ϵ_r) values as a function of the composition x of the synthesized $\text{Ca}_{2-x}\text{Cu}_x\text{P}_2\text{O}_7$ ($x = 0.00\text{--}2.00$) are presented in Fig. 6, which shows the combination values between the calculated data (atomic polarization part, red bars) and measured results (atomic polarization part + ionic polarization part, red and purple bars). The single metal pyrophosphates ($\text{Ca}_2\text{P}_2\text{O}_7$ and $\text{Cu}_2\text{P}_2\text{O}_7$) showed ϵ_r values of 15.6 and 10.5, respectively, which were higher than the ϵ_r value of binary metal pyrophosphates (i.e., CaCuP_2O_7 , $\epsilon_r = 9.8$). The ϵ_r values of the mixing phases of binary metal pyrophosphates ($\text{Ca}_{1.50}\text{Cu}_{0.50}\text{P}_2\text{O}_7$ and 1.50 ($\text{Ca}_{0.50}\text{Cu}_{1.50}\text{P}_2\text{O}_7$)) have not been estimated because of the unknown amount of exact phase composition. The Clausius-Mossotti equation focused on only the dielectric constant from atomic polarization (electron cloud bias in electric fields). Indeed, the samples were measured at a frequency of 1 MHz for the decreasing extrinsic factor, and the polarization caused the movement of both cations (Cu^{2+} , Ca^{2+} , and P^{5+}) and anions (O^{2-}) in the crystal $\text{Ca}_{2-x}\text{Cu}_x\text{P}_2\text{O}_7$ structure. The movement of the ions in the electric field was caused

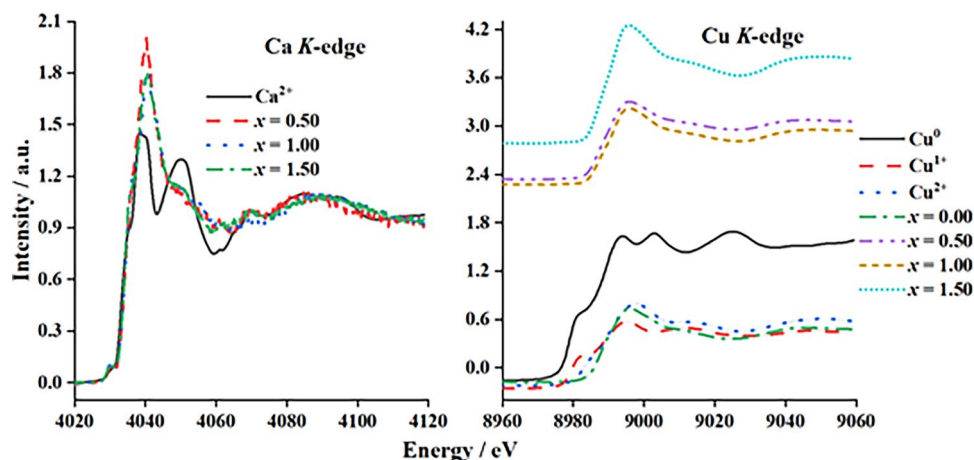


Figure 7. Extended X-ray absorption fine structure (EXAFS) spectra of Cu^0 , Cu^{1+} , Cu^{2+} , Ca^{2+} , and $\text{Ca}_{2-x}\text{Cu}_x\text{P}_2\text{O}_7$; $x = 0.00$ – 1.50 .

x values	Compounds	Path	Shell	CN	R / Å	σ^2 / Å ²	R-factor
2.00	$\text{Cu}_2\text{P}_2\text{O}_7$	Cu–O _{eq}	1	2	1.90505	0.00508	0.00369
		Cu–O _{eq}	1	2	1.96427	0.00499	
		Cu–O _{ax}	1	1	2.30075	0.03223	
		Cu–O _{ax}	2	1	2.91358	0.00796	
1.00	CaCuP_2O_7	Cu–O _{eq}	1	1	1.88239	0.05892	0.01308
		Cu–O _{eq}	1	2	1.94469	0.00529	
		Cu–O _{eq}	1	1	1.99797	0.06324	
		Cu–O _{ax}	1	1	2.15606	0.33359	
		Cu–O _{ax}	2	1	2.88853	0.00839	

Table 3. Bond length from EXAFS fitting for $\text{Ca}_{2-x}\text{Cu}_x\text{P}_2\text{O}_7$ samples; $x = 1.00$ and 2.00 . where eq and ax subscripts are equatorial and axial (or apical) positions, respectively. CN is the coordination number, R is the radial distance, σ^2 is the mean squared displacement, and the R-factor is the fitting statistic factor.

by an increasing dielectric constant compared to the calculated data using the Clausius-Mossotti equation. The equation used in this study considered the dielectric constant, using the bond angle, bond length, and volume of the MO_6 octahedra.

The extended X-ray absorption fine structure (EXAFS) spectra of the synthesized $\text{Ca}_{2-x}\text{Cu}_x\text{P}_2\text{O}_7$ samples are shown in Fig. 7. The environment around Cu atoms was investigated. The primitive EXAFS model was taken from parameters obtained from the Rietveld refinement of each sample.

Details of the EXAFS spectroscopic fitting of the $\text{Ca}_{2-x}\text{Cu}_x\text{P}_2\text{O}_7$ samples are summarized in Table 3, which shows the distortion of the CuO_6 octahedra. The spectra of $x = 0.00$ were undetectable because of the limitation of the instrument in beamline 8 of the National Synchrotron Research Center (Thailand). As presented in Table 3, the samples, when $x = 1.00$ and 2.00 , showed three main shells. The first shell of the spectrum from the model consisted of four equatorial oxygen atoms, Cu–O_{1eq}, Cu–O_{2eq}, Cu–O_{3eq}, and Cu–O_{4eq}, of the CuO_6 octahedral. Then, the second shell detected only one axial oxygen atom, Cu–O_{5ax}. The last axial oxygen atom, Cu–O_{6ax}, was observed in the third shell. The Cu atoms of Cu–O₆ were also combined with the phosphorus atom Cu–P. Different radial distances (R/Å) between the Rietveld refinement and EXAFS fitting may be the cause of the measurement type of each technique. X-ray diffraction (Rietveld refinement) was used to investigate the global structure, while X-ray absorption (EXAFS fitting) was used to probe the details of the Cu/Ca local structure^{42,43}. The fitting statistic factor (R-factor) of $x = 1.00$ was worse than that of $x = 2.00$ because of two important factors. First, the crystal structure of $\alpha\text{-CaCuP}_2\text{O}_7$ ($x = 1.00$) was less symmetric than that of another sample ($\text{Cu}_2\text{P}_2\text{O}_7$ ($x = 1.00$)). Second, $\alpha\text{-CaCuP}_2\text{O}_7$ ($x = 1.00$) exhibited four different types of atomic positions in the unit cell.

Vibrational spectroscopy. FTIR and Raman spectroscopies are good methods for identifying the chemical bonding of rotational, vibration, and other low-frequency modes in the phosphate group⁴⁴. After applying the Spectrum GX FTIR spectrometer, the FTIR spectra of the synthesized $\text{Ca}_{2-x}\text{Cu}_x\text{P}_2\text{O}_7$ samples are presented in Fig. 8, whereas the corresponding assignments are tabulated in Table 4. The FTIR spectra observed in this research are similar to the spectral results reported in the literature^{12,13,15–17,45}. They successfully synthesized and investigated the vibrational spectroscopy of various single, double, and triple metal pyrophosphates, i.e., $\text{Mg}_2\text{P}_2\text{O}_7$, $\text{Mn}_{1.8}\text{Co}_{0.2}\text{P}_2\text{O}_7$, $\text{Mn}_{1.8}\text{Co}_{0.1}\text{Mg}_{0.1}\text{P}_2\text{O}_7$, $\text{Co}_{1.6}\text{Zn}_{0.2}\text{Mn}_{0.2}\text{P}_2\text{O}_7$, and CoFeP_2O_7 .

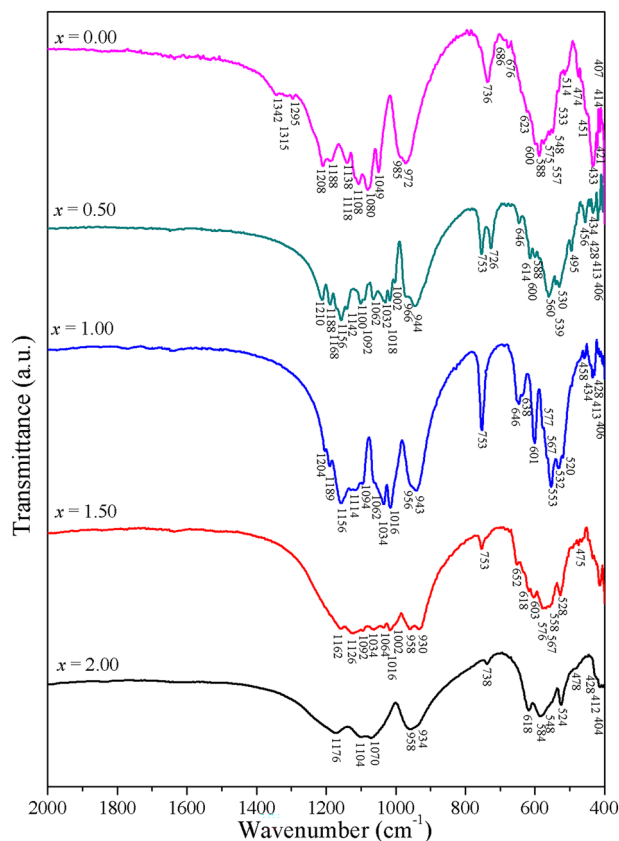


Figure 8. Fourier transform infrared (FTIR) spectra of the synthesized $\text{Ca}_{2-x}\text{Cu}_x\text{P}_2\text{O}_7$; $x = 0.00\text{--}2.00$.

Compounds	Wavenumber/ cm^{-1}	FTIR	Raman	Assignments
$\text{Ca}_{2-x}\text{Cu}_x\text{P}_2\text{O}_7$; $x = 0.00\text{--}2.00$	1250–1200	NO	Weak	α -phase characteristics
	1200–1100	Very strong	Very strong	$\nu_{\text{as}}\text{PO}_3$
	1100–1050	Very strong	Very strong	$\nu_s\text{PO}_3$
	1050–1000	Very strong	Very strong	$\nu_{\text{as}}\text{PO}_3$
	980–950	Strong	Very weak	$\nu_{\text{as}}\text{P-O-P}$
	760–730	Medium	Weak	$\nu_s\text{P-O-P}$
	650–280	Strong	Strong	$\delta\text{OPO} + \nu_s\text{M-O}$
	260–160	NO	Weak	$\nu_s\text{M-O}$
200–100	NO	Medium	Lattice vibration	

Table 4. Vibrational positions (wavenumber / cm^{-1}) and vibrational assignments (modes) of the synthesized $\text{Ca}_{2-x}\text{Cu}_x\text{P}_2\text{O}_7$ samples obtained from the FTIR and Raman techniques. NO is not observed.

The vibrational characteristics of the synthesized $\text{Ca}_{2-x}\text{Cu}_x\text{P}_2\text{O}_7$ are described in detail. The strong vibrational bands at approximately 1190 and 1060 cm^{-1} were attributed to an asymmetric ($\nu_{\text{as}}\text{PO}_3$) vibrational mode of the PO_3 unit of the pyrophosphate ($\text{O}_3\text{P-O-PO}_3^{4-}$ or $\text{P}_2\text{O}_7^{4-}$) ions, whereas a vibrational band at approximately 1100 cm^{-1} was attributed to the symmetric stretching ($\nu_s\text{PO}_3$) of the PO_3 unit. The asymmetric ($\delta_{\text{as}}\text{PO}_3$) and symmetric ($\delta_s\text{PO}_3$) bending modes are observed at the vibrational positions at approximately 580 and 540 cm^{-1} , respectively. The asymmetric ($\nu_{\text{as}}\text{P-O-P}$) and symmetric stretching ($\nu_s\text{P-O-P}$) modes of the P-O-P bridge of the $\text{O}_3\text{P-O-PO}_3^{4-}$ group were observed at vibrational positions of approximately 960 and 740 cm^{-1} , respectively. However, in the case of the $\text{Ca}_{2-x}\text{Cu}_x\text{P}_2\text{O}_7$ samples with $x = 0.50$ ($\text{Ca}_{1.5}\text{Cu}_{0.5}\text{P}_2\text{O}_7$) and $x = 1.5$ ($\text{Ca}_{0.5}\text{Cu}_{1.5}\text{P}_2\text{O}_7$), the P-O-P symmetric stretching mode appeared as two peaks in the range of 776–693 cm^{-1} , which corresponded to the vibrational characteristics (symmetric stretching) of the P-O-P bridge. These detected peaks may be due to the mixing phases of the metal pyrophosphate compounds, i.e., $\text{Ca}_2\text{P}_2\text{O}_7$ and CuCaP_2O_7 . In addition, the rocking mode of the P-O-P deformations and the torsional and external modes were found in the 450–410 cm^{-1} regions.

The Raman spectroscopic technique was additionally applied to investigate and support the FTIR results, especially the vibrational spectroscopy of the metal oxide (M-O) bond as well as the lattice vibration by observation in the low frequency range (650–100 cm^{-1}). Furthermore, the phase characteristics (α -, β -phases) of the

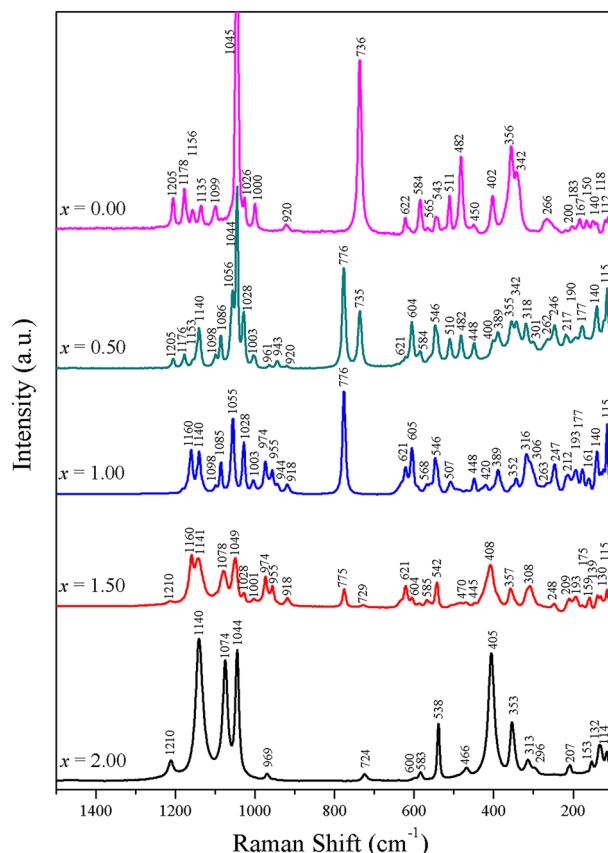


Figure 9. Raman spectra of the synthesized $\text{Ca}_{2-x}\text{Cu}_x\text{P}_2\text{O}_7$ compounds when $x=0.00\text{--}2.00$.

metal pyrophosphate compounds can be observed from this spectroscopic technique. After applying the DXR Raman microscope, the Raman spectra of the samples are shown in Fig. 9, and the corresponding vibrational assignments are listed in Table 4. It was observed that the result corresponded well to the FTIR result. The Raman results showed the specific phase, which formed at high temperature in pyrophosphate with $x = 1.00$ (CaCuP_2O_7), as described in the literature⁴⁶ through an undetectably weak peak at approximately 1210 cm^{-1} . The three distinct peaks of $\text{Ca}_{2-x}\text{Cu}_x\text{P}_2\text{O}_7$, where $x = 0.00, 0.50, 1.50$ and 2.00 , which originated from the $\nu_{\text{as}}\text{PO}_3$ vibrational characteristics, were observed and found to be at approximately $1210, 1140$ and 1080 cm^{-1} . The Raman spectra clearly showed that the studied metal pyrophosphates displayed sharpness and splitting, especially in the investigated frequency region ($1300\text{--}100\text{ cm}^{-1}$). The vibrational analysis of the $\text{P}_2\text{O}_7^{4-}$ ion, which contained the O–P–O radical (PO_2^- of $\text{O}_2\text{O–P–OPO}_3^{4-}$) and the P–O–P bridge (of $\text{O}_3\text{P–O–PO}_3^{4-}$), was exhibited in the Raman spectra. Moreover, M–O stretching and phase characteristics were also observed. The Raman spectra observed in this research were similar to the spectra reported by Sronsri et al.^{12,13,15–17} and Boonchom et al.⁴⁵ The strong vibrational band at approximately 1100 cm^{-1} was attributed to the stretching of the PO_3 unit of $\text{O}_3\text{P–O–PO}_3^{4-}$. The asymmetric ($\nu_{\text{asym}}\text{POP}$) and symmetric ($\nu_{\text{sym}}\text{POP}$) stretching types of the P–O–P bridge of $\text{O}_3\text{P–O–PO}_3^{4-}$ were detected at approximately 960 and 730 cm^{-1} , respectively. The asymmetric ($\delta_{\text{asym}}\text{PO}_3$) and symmetric ($\delta_{\text{sym}}\text{PO}_3$) vibrational bending modes of $\text{O}_3\text{P–O–PO}_3^{4-}$ were observed at approximately 600 and 520 cm^{-1} , respectively.

Dielectric and optical properties. *Structural-dielectric relation.* The bond angle and bond length were successfully investigated by using the Rietveld refinement technique, as shown in Table 1. The obtained refinement results were then used to describe the phenomena of the dielectric properties of the samples. In general, the dielectric properties of the metal pyrophosphate ($\text{M}_2\text{P}_2\text{O}_7$) group occurred from two important effects, which consisted of O-atom shifting in the collinear P–O–P bridge and M^{2+} -ion movement in the MO_6 octahedral. According to previous works, due to the shifting of the O atom in the collinear P–O–P bridge, the P–O–P bond angles of $\text{Ca}_2\text{P}_2\text{O}_7$ and $\text{Cu}_2\text{P}_2\text{O}_7$ of 130° ⁴⁷ and 157° ⁴⁸ were reported, respectively. In this section, only three synthesized $\text{Ca}_{2-x}\text{Cu}_x\text{P}_2\text{O}_7$ samples, when $x = 0.00, 1.00$, and 2.00 , were considered. The sample, when $x = 0.00$ ($\text{Ca}_2\text{P}_2\text{O}_7$), showed two different P–O–P bond angles. First, a bond angle of 116.52° appeared for 4 clusters per unit cell with asymmetric P–O bond lengths of 1.765 \AA and 1.887 \AA . Second, a P–O–P bond angle of 140.96° appeared for 4 clusters per unit cell with symmetric P–O bond lengths of 1.536 \AA and 1.827 \AA . The sample, when $x = 2.00$ ($\text{Cu}_2\text{P}_2\text{O}_7$), had a P–O–P bond angle of 154.6° and 4 clusters per unit cell with a symmetric P–O bond length of 1.574 \AA . Pogorzelec-Glaser et al.⁴⁶ reported that at high temperature, the binary metal pyrophosphate ($\text{CuM}^{2+}\text{P}_2\text{O}_7$) compounds crystallized in a monoclinic crystal system with the space group of $\text{C}2/m$, and the P–O–P angle was linear (180°). The sample, when $x = 1.00$ (CaCuP_2O_7), exhibited the space group of $\text{P}2_1/n$.

x values	Compounds	Average bond lengths/Å	Octahedral volumes/Å ³	Distortion index
2.00	Cu ₂ P ₂ O ₇	2.1794	12.6198	0.1400
1.00	CaCuP ₂ O ₇	2.4032	15.9050	0.0886
0.00	Ca ₂ P ₂ O ₇	2.4479	18.6696	0.0655

Table 5. Average bond length, octahedral volume, and distortion index of Ca_{2-x}Cu_xP₂O₇ samples ($x=0.00$, 1.00, and 2.00).

The refinement result showed a P–O–P bond angle of 159.00° and 4 clusters per unit cell with asymmetric P–O bond lengths of 1.592 Å and 1.521 Å. However, the number of P–O–P clusters in each Ca_{2-x}Cu_xP₂O₇ sample ($x=0.00$, 1.00, and 2.00) was equal (4). Based on these obtained results, the P–O–P cluster number did not affect the polarization of the samples.

The single metal pyrophosphate, when $x = 0.00$ (Ca₂P₂O₇), showed an outstanding dielectric constant (15.6, as shown in Fig. 6). This was a very high polarization; it therefore caused and made the narrow P–O–P bond angle. In addition, the long P–O bond length of the sample of $x = 0.00$ (Ca₂P₂O₇), resulting in weak bonding, was better than the samples of $x = 1.00$ (CaCuP₂O₇) and $x = 2.00$ (Cu₂P₂O₇). Additionally, the volume of the octahedral coordination was calculated using the method reported by Swanson et al.⁴⁹ to present the relationship between the polarization and metal oxide bonding. In addition, the distortion index (D) was used to describe the distortion of the sample crystal structure. Baur⁵⁰ described the calculation of the D value based on the bond lengths, as shown in Eq. (5).

$$D = \frac{1}{n} \sum_{i=1}^n \frac{|l_i - l_{av}|}{l_{av}} \quad (5)$$

where l_{av} is the average bond length and l_i is the atomic distance from the central atom to the i th coordinating atom.

The refinement analysis results also showed a change in the average M–O bond lengths in the MO₆ octahedral site, which caused molecular polarization. As demonstrated in Table 5, both the average bond lengths and octahedral volumes decreased with increasing x values. However, a different result was observed for the distortion index. The distortion index values increase with increasing x values, which then decreases the molecular polarization, resulting in a decrease in the dielectric constant (ϵ_r). These analyses showed that the polarization of Ca_{2-x}Cu_xP₂O₇ occurred due to O shifting in the collinear P–O–P bridge, which is the main factor in the generation of a narrow bond angle that causes high polarization and a high dielectric constant. Moreover, the movement of M²⁺ ions in the MO₆ octahedral was a supplementary factor, in which the longer average M–O bond length and larger octahedral volume led to the high polarization and high dielectric constant of the materials.

Structural-optical relation. The distortion of the MO₆ octahedral can increase the Cu–O₆ bond lengths of Ca_{2-x}Cu_xP₂O₇, resulting in an increase in the octahedral crystal field splitting energy (Δ_0 , please see Fig. 10). The Δ_0 values of the synthesized Ca_{2-x}Cu_xP₂O₇ samples ($x=0.50$ – 2.00) are listed in Table 6.

As presented in Table 6, Δ_0 increased with increasing Cu²⁺ fraction in the Ca_{2-x}Cu_xP₂O₇ compound, and when $x = 2$ (Cu₂P₂O₇), the highest Δ_0 value was obtained. The compounds illustrated the change in color from blue-green to bluish-green. The colorless compound, when $x = 0.00$ (Ca₂P₂O₇), was due to the fulfillment state in the octet rule of Ca²⁺ ions in the structure, despite the distortion appearing in the CaO₆ octahedral site. The octahedral splitting diagram of Ca_{2-x}Cu_xP₂O₇; $x = 0.50$ – 2.00 is summarized and presented in Fig. 10. Total interpretations showed that the MO₆ octahedral distortion affected both the color of the sample and the polarization of the octahedral unit, as reflected in the dielectric constant of the compounds.

Conclusions

Binary metal pyrophosphates (Ca_{2-x}Cu_xP₂O₇) were successfully synthesized via a solid-state reaction process. The synthesized Ca_{2-x}Cu_xP₂O₇ samples were systematically characterized by various scientific instruments. The structural analysis exhibits the single solid phase for the obtained Ca₂P₂O₇, CaCuP₂O₇, and Cu₂P₂O₇ samples and the mixing solid phases for the obtained Ca_{1.5}Cu_{0.5}P₂O₇ and Ca_{0.5}Cu_{1.5}P₂O₇ samples. The tetragonal crystal system with the $P4_1$ space group is a crystal for β -Ca₂P₂O₇, while the monoclinic crystal systems with the $P2_1/c$ and $C2/c$ space groups are crystals for CaCuP₂O₇ and α -Cu₂P₂O₇, respectively. The color of the samples changed from yellowish-green to bluish-green when the Cu content increased because the absorption wavelength increased and corresponded to a decrease in the z-axis expansion. Using the Rietveld refinement method, the P–O–P bond angle and P–O bond length and details of the octahedral MO₆ (the average bond length, octahedral volume, and distortion index) were calculated. The addition of Cu²⁺ ions in the Ca₂P₂O₇ structure resulting in distortion of the crystal structure affected the changes in the bond length and bond angle of the P–O–P groups in the P₂O₇⁴⁻ ions and the octahedral volume and average bond lengths in the octahedral MO₆ site. Shifting O atoms in the collinear P–O–P bridge (a narrow bond angle) and the movement of M²⁺ ions in octahedral MO₆ (the longer average M–O bond length and larger octahedral volume) are probably the main factors leading to the high values of polarization and dielectric constant of metal pyrophosphates. Finally, these results illustrated that the distortion of the octahedral MO₆ resulted in a straightway effect on the color of the metal pyrophosphate compounds, while the change in the P–O–P bridge influenced the dielectric properties.

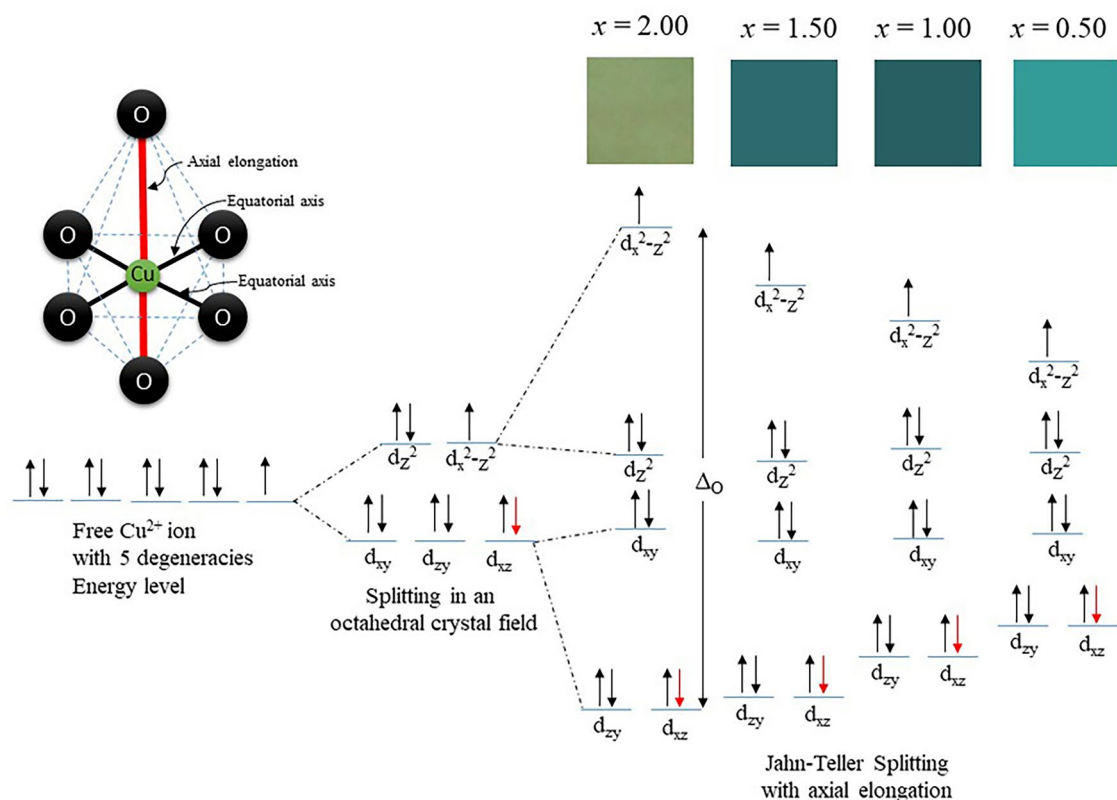


Figure 10. Octahedral splitting diagram of the synthesized $\text{Ca}_{2-x}\text{Cu}_x\text{P}_2\text{O}_7$ samples; $x = 0.50\text{--}2.00$.

x values	Compounds	Wavelengths/nm		$\Delta_0/\text{kJ}\cdot\text{mol}^{-1}$	Cu–O _{ax} bond lengths/Å	
		Observed	Absorbed		XRD	EXAFS
2.00	$\text{Cu}_2\text{P}_2\text{O}_7$	561	403	297	2.92	2.91
1.50	$\text{Ca}_{0.5}\text{Cu}_{1.5}\text{P}_2\text{O}_7$	488	642	186	ND	ND
1.00	CaCuP_2O_7	489	644	185	2.81	2.89
0.50	$\text{Ca}_{1.5}\text{Cu}_{0.5}\text{P}_2\text{O}_7$	492	648	184	ND	ND
0.00	$\text{Ca}_2\text{P}_2\text{O}_7$	ND	ND	ND	ND	ND

Table 6. Approximate wavelength of the energy absorption. *ND* is not detected.

Received: 28 January 2022; Accepted: 18 April 2022

Published online: 27 April 2022

References

- Bian, J., Kim, D. & Hong, K. Microwave dielectric properties of $(\text{Zn}_{1-x}\text{Mn}_x)_2\text{P}_2\text{O}_7$. *J. Mater. Sci.* **40**, 1801–1803 (2005).
- Bian, J.-J., Kim, D.-W. & Hong, K. S. Microwave Dielectric Properties of $\text{A}_2\text{P}_2\text{O}_7$ (A = Ca, Sr, Ba; Mg, Zn, Mn). *Jpn. J. Appl. Phys.* **43**, 3521 (2004).
- Wenwei, W., Yanjin, F., Xuehang, W., Sen, L. & Shushu, L. Preparation via solid-state reaction at room temperature and characterization of layered nanocrystalline $\text{NH}_4\text{MnPO}_4 \cdot \text{H}_2\text{O}$. *J. Phys. Chem. Solids* **70**, 584–587 (2009).
- Weil, M. & Stöger, B. Crystal chemistry of transition metal diarsenates $\text{M}_2\text{As}_2\text{O}_7$ (M = Mn, Co, Ni, Zn): Variants of the thortveitite structure. *Acta Crystallogr. B* **66**, 603–614 (2010).
- Sebastian, M.T. *Dielectric Materials for Wireless Communication*. (Elsevier, 2010).
- Chapman, R., Mercer, I., Rankin, A., Spratt, J. Thortveitite—a new gemstone. *Gemmology* **1** (2004).
- Livitska, O., Strutynska, N., Livitska, O., Slobodyanik, N. The alternative approach to the preparation of complex calcium phosphates and their characterization. *Funct. Mater.* (2017).
- Ranby, P., Mash, D. & Henderson, S. The investigation of new phosphors, with particular reference to the pyrophosphates. *Br. J. Appl. Phys.* **6**, S18 (1955).
- Lin, F.-H., Liaw, J.-R., Hon, M.-H. & Wang, C.-Y. The effects of $\text{Na}_4\text{P}_2\text{O}_7 \cdot 10\text{H}_2\text{O}$ addition on the mechanical properties of sintered $\text{Ca}_2\text{P}_2\text{O}_7$ bioceramic. *Mater. Chem. Phys.* **41**, 110–116 (1995).
- Bian, J., Kim, D. & Hong, K. Microwave dielectric properties of $(\text{Ca}_{1-x}\text{Zn}_x)_2\text{P}_2\text{O}_7$. *Mater. Lett.* **59**, 257–260 (2005).
- Bian, J.-J., Kim, D.-W. & Hong, K. S. Glass-free LTCC microwave dielectric ceramics. *Mater. Res. Bull.* **40**, 2120–2129 (2005).

12. Sronsri, C., Sittipol, W. & Kongpop, U. Optimization of biodiesel production using magnesium pyrophosphate. *Chem. Eng. Sci.* **226**, 115884 (2020).
13. Sronsri, C., Noisong, P. & Danvirutai, C. Thermal decomposition kinetics of Mn 0.9 Co 0.1 HPO₄ · 3H₂O using experimental-model comparative and thermodynamic studies. *J. Therm. Anal. Calorim.* **127**, 1983–1994 (2017).
14. Riou, D. & Goreaud, M. CaCu₂P₂O₇: a structure closely related to α-Ca₂P₂O₇. *Acta Crystallogr. C* **46**, 1191–1193 (1990).
15. Sronsri, C. & Boonchom, B. Thermal kinetic analysis of a complex process from a solid-state reaction by deconvolution procedure from a new calculation method and related thermodynamic functions of Mn_{0.9}Co_{0.05}Mg_{0.05}HPO₄ · 3H₂O. *Trans. Nonferrous Metals Soc. China* **28**, 1887–1902 (2018).
16. Sronsri, C. Thermal dehydration kinetic mechanism of Mn_{1.8}Co_{0.1}Mg_{0.1}P₂O₇·2H₂O using Málek's equations and thermodynamic functions determination. *Trans. Nonferrous Metals Soc. China* **28**, 1016–1026 (2018).
17. Sronsri, C., Noisong, P. & Danvirutai, C. Isoconversional kinetic, mechanism and thermodynamic studies of the thermal decomposition of NH₄ Co_{0.8} Zn_{0.1} Mn_{0.1} PO₄ H₂ O. *J. Therm. Anal. Calorim.* **120**, 1689–1701 (2015).
18. Xiao, Z. W., Hu, G. R., Peng, Z. D., Du, K. & Gao, X. G. Solid state synthesis and characterization of iron(II) pyrophosphate Fe₂P₂O₇. *Chin. Chem. Lett.* **18**, 1525–1527 (2007).
19. Bensalem, A., Ahluwalia, M., Vijayaraghavan, T. V. & Ko, Y. H. Synthesis of amorphous MgHPO₄ x(R) [R = Ethanol; Ethylene glycol] in anhydrous media. *Mater. Res. Bull.* **32**, 1473–1483 (1997).
20. Díaz, C. *et al.* Nanostructured copper oxides and phosphates from a new solid-state route. *Inorg. Chim. Acta* **377**, 5–13 (2011).
21. Sronsri, C., Danvirutai, C. & Noisong, P. Double function method for the confirmation of the reaction mechanism of LiCoPO₄ nanoparticle formation, reliable activation energy, and related thermodynamic functions. *React. Kinet. Mech. Catal.* **121**, 555–577 (2017).
22. Brandová, D., Trojan, M., Arnold, M., Paulik, F. & Paulik, J. Mechanism of dehydration and condensation of CuHPO₄ · H₂O. *J. Therm. Anal.* **34**, 1449–1454 (1988).
23. Brandová, D., Trojan, M., Paulik, F. & Paulik, J. Mechanism of dehydration of ZnHPO₄ · H₂O. *J. Therm. Anal.* **32**, 1923–1928 (1987).
24. Jouini, A., Gâcon, J. C., Ferid, M. & Trabelsi-Ayadi, M. Luminescence and scintillation properties of praseodymium poly and diphosphates. *Opt. Mater.* **24**, 175–180 (2003).
25. Yang, T. & Lin, J. Hydrothermal syntheses and low temperature magnetic behaviors of ACo₃(P₂O₇)₂ (A=Ca, Sr, Ba, Pb). *J. Solid State Chem.* **198**, 1–5 (2013).
26. Sronsri, C., Sittipol, W. & Kongpop, U. Luminescence characterization of Mn-doped LiMgPO₄ synthesized using different precursors. *J. Solid State Chem.* **297**, 122083 (2021).
27. Kim, C. H. & Yim, H. S. The effect of tetravalent metal on dielectric property in ZrP₂O₇ and TiP₂O₇. *Solid State Commun.* **110**, 137–142 (1999).
28. Shannon, R. Revised effective ionic radii and systematic studies of interatomic distances in halides and chalcogenides. *Acta Crystallogr. A* **32**, 751–767 (1976).
29. Klysubun, W., Sombunchoo, P., Deenan, W. & Kongmark, C. Performance and status of beamline BL8 at SLRI for X-ray absorption spectroscopy. *J. Synchrotron Radiat.* **19**, 930–936 (2012).
30. Rietveld, H. A profile refinement method for nuclear and magnetic structures. *J. Appl. Crystallogr.* **2**, 65–71 (1969).
31. Rodríguez-Carvajal, J. Recent advances in magnetic structure determination by neutron powder diffraction. *Physica B* **192**, 55–69 (1993).
32. Robertson, B. E. & Calvo, C. Crystal structure of β-Cu₂P₂O₇. *Can. J. Chem.* **46**, 605–612 (1968).
33. Ferraro, J. *Introductory Group Theory and its Application to Molecular Structure*. (Springer Science and Business Media, 2012).
34. Yano, J. & Yachandra, V. K. X-ray absorption spectroscopy. *Photosynth. Res.* **102**, 241–254 (2009).
35. Myung, S. T. *et al.* Emulsion drying preparation of layered LiMnCr_{1-x}O₂ solid solution and its application to Li-ion battery cathode material. *J. Power Sources* **119**, 211–215 (2003).
36. El Jazouli, A., Tbib, B., Demourgues, A. & Gaudon, M. Structure and colour of diphosphate pigments with square pyramid environment around chromophore ions (Co²⁺, Ni²⁺, Cu²⁺). *Dyes Pigm.* **104**, 67–74 (2014).
37. Chen, L.-T., Hwang, C.-S., Sun, I. L. & Chen, I.-G. Luminescence and chromaticity of alkaline earth aluminate M_xSr_{1-x}Al₂O₄:Eu²⁺ (M: Ca, Ba). *J. Lumin.* **118**, 12–20 (2006).
38. Kukliński, B. *et al.* Luminescent GeO₂-Pb-Bi₂O₃ glasses co-doped with Tb³⁺ and Eu³⁺: Excitation energy transfer and color chromaticity. *Opt. Mater.* **36**, 633–638 (2014).
39. Kim, B.-K. & Park, R.-H. Detection and correction of purple fringing using color desaturation in the xy chromaticity diagram and the gradient information. *Image Vis. Comput.* **28**, 952–964 (2010).
40. Sebastian, M. T. *Dielectric materials for wireless communication*. xiii, 671 p., 2 p. of plates (Amsterdam, Boston, Elsevier, 2008).
41. Bosman, A. J. & Havinga, E. E. Temperature dependence of dielectric constants of cubic ionic compounds. *Phys. Rev.* **129**, 1593–1600 (1963).
42. Voronin, V. I. *et al.* Neutron diffraction, synchrotron radiation and EXAFS spectroscopy study of crystal structure peculiarities of the lanthanum nickelates Laⁿ⁺¹NiⁿO₉ (n=1,2,3). *Nucl. Instrum. Methods Phys. Res., Sect. A* **470**, 202–209 (2001).
43. Yingjie, L. *et al.* EXAFS study of Mn_{1.28}Fe_{0.67}P_{0.46}Si_{0.54} compound with first-order phase transition. *J. Electron Spectrosc. Relat. Phenom.* **196**, 104–109 (2014).
44. Sronsri, C. & Boonchom, B. Synthesis, characterization, vibrational spectroscopy, and factor group analysis of partially metal-doped phosphate materials. *Spectrochim. Acta Part A Mol. Biomol. Spectrosc.* **194**, 230–240 (2018).
45. Boonchom, B. & Phuvongpha, N. Synthesis of new binary cobalt iron pyrophosphate CoFeP₂O₇. *Mater. Lett.* **63**, 1709–1711 (2009).
46. Pogorzelec-Glaser, K., Pietraszko, A., Hilczer, B. & Polomska, M. Structure and phase transitions in Cu₂P₂O₇. *Phase Trans.* **79**, 535–544 (2006).
47. Robertson, B. E. & Calvo, C. The crystal structure and phase transformation of [α]-Cu₂P₂O₇. *Acta Crystallogr. A* **22**, 665–672 (1967).
48. Bian, J.-J., Kim, D.-W. & Hong, K. S. Microwave dielectric properties of Ca₂P₂O₇. *J. Eur. Ceram. Soc.* **23**, 2589–2592 (2003).
49. Swanson, D. K. & Peterson, R. C. Polyhedral volume calculations. *Can. Mineral.* **18**, 153–156 (1980).
50. Baur, W. The geometry of polyhedral distortions. Predictive relationships for the phosphate group. *Acta Crystallogr. Sect. B* **30**, 1195–1215 (1974).

Acknowledgements

This work is supported by King Mongkut's Institute of Technology Ladkrabang [KREF146002]. The authors would like to thank the Scientific Instruments Center KMITL for supporting the TGA, FTIR, XRD, and SEM techniques.

Author contributions

R.B. carried out the experiments and analysis. C.S. and S.T. contributed to the characterization and analysis. K.C. and S.T. contributed to the experiments and analysis and approved the main manuscript text. N.M. approved the main manuscript text. B.B. designed the study, contributed to the experiments and analysis and wrote the

main manuscript text. All the authors analyzed the results, contributed to discussion and contributed to writing the manuscript.

Competing interests

The authors declare no competing interests.

Additional information

Correspondence and requests for materials should be addressed to S.T. or B.B.

Reprints and permissions information is available at www.nature.com/reprints.

Publisher's note Springer Nature remains neutral with regard to jurisdictional claims in published maps and institutional affiliations.



Open Access This article is licensed under a Creative Commons Attribution 4.0 International License, which permits use, sharing, adaptation, distribution and reproduction in any medium or format, as long as you give appropriate credit to the original author(s) and the source, provide a link to the Creative Commons licence, and indicate if changes were made. The images or other third party material in this article are included in the article's Creative Commons licence, unless indicated otherwise in a credit line to the material. If material is not included in the article's Creative Commons licence and your intended use is not permitted by statutory regulation or exceeds the permitted use, you will need to obtain permission directly from the copyright holder. To view a copy of this licence, visit <http://creativecommons.org/licenses/by/4.0/>.

© The Author(s) 2022